Self-driven intelligent curved hinge based on shape-morphing composites

Xiaozhou Xin [a], Cheng Lin [b], Bingxun Li [a], Chengjun Zeng [a], Liwu Liu [a,*], Yanju Liu [a,*], Jinsong Leng [b]

[a] *Department of Astronautical Science and Mechanics, Harbin Institute of Technology (HIT), P.O. Box 301, No. 92 West Dazhi Street, Harbin 150001, People's Republic of China*
[b] *Center for Composite Materials and Structures, Harbin Institute of Technology (HIT), P.O. Box 3011, No. 2 Yikuang Street, Harbin 150080, People's Republic of China*

ARTICLE INFO

ABSTRACT

The space deployable structures based on shape memory polymer composites (SMPCs) possessed excellent self-deployable performance, which effectively avoided the impact and electromagnetic pulse (EMP) caused by the explosion of pyrotechnic devices. In this work, two types of self-driven curved hinges with different angles of 80° and 115° (Type 80 and Type 115) were designed based on SMPCs. The thermomechanical properties and time–temperature-dependent viscoelastic behaviors of SMPCs were systematically investigated. The three-point bending performance and cyclic shape memory performance of the developed hinges were also characterized. In addition, the deployment performances of Type 80 driven 350 g object under different heating powers were investigated in the environment of $\pm$ 70 °C and 10^3 Pa atmospheric pressure. A staircase-like heating strategy was proposed to achieve precise and controllable deployment under this environment. The developed self-driven curved hinges were expected to have tremendous application potential on the flap actuators and optical payload rotating platforms of the satellites.

1. Introduction

Shape memory polymers (SMPs) were a type of intelligent materials that possessed the ability to maintain the programmed temporary shape and recover to its original shape under specific environmental stimuli (e. g., thermal, electrical, and magnetic). [1–10] Shape memory polymer composites have been developed to improve driving force, thermo-mechanical properties and viscoelastic properties by incorporating functional particles or fibers into SMPs.[11–13] Due to the various driving methods and impact lessness during the deployment process, SMPCs have attracted great interests in space. [8,14–17].

In the design of spacecraft, the separation of substructure system (e. g., payload separation from launch vehicle) and deployable structure (e. g., solar array, antenna) were usually accomplished by the pyrotechnic device (e.g., explosive bolt and mild linear shaped charge). The pyro shock and vibration caused by the start-up of these devices were one of the most severe mechanical environments experienced by spacecraft. In addition, electromagnetic pulse (EMP) generated by ionization of surrounding air during the explosion also interfered with electronic equipment. According to the survey of NASA, more than 71 % of flight faults between 1963 and 1985 were caused by pyrotechnic. [18].

The micro-buckling of the SMPCs increased the storage ratio of space deployable structures, providing solutions for the transportation and packaging of large structures. [19] CTD (Composite Technology Development, Inc.) designed a hinge that can be electrothermally deployed, and the hinge was optimized to achieve greater driving force. [20,21] Lan et al. completed the experiment for driving solar array using SMPCs-based hinge, the deployment time was 80 s. [19] Dao et al. introduced a method for measuring the blocking force of SMPCs-based space deployable hinges to quantify their performance. [22] In addition, more complex SMPCs-based structures were designed. The deployable beam structure was designed by CTD to meet the needs of micro-satellite. [23] Complex tri-longitudinal beam [24] and tetrahedral truss [25] have also attracted wide attention due to their small vibration response and high stiffness. Keller et al. developed a deployable high-precision antenna for NASA's Mars exploration mission. [26] Chen et al. designed a space-deployable mechanism (SDM) by SMPCs and composite spring tapes. [27] Liu et al. prepared the integrated hinge structure without complicated mechanical connections, which was expected to be used in space capture and multi-angle imaging systems. [28] Liu et al. designed a lenticular collapsible composite tube (LCCT) for flexible solar array. Compared with traditional LCCT, SMPCs-based LCCT exhibited the

advantages of lightweight, foldability, stable and controllable deployment. [29] Lan et al. developed a deployable SMPC flexible solar array system (SMPC-FSAS), which was launched on December 27, 2019 on the SJ20 geostationary orbit satellite. On January 5, 2020, it successfully unlocked and achieved a shape recovery ratio of nearly 100 % within 60 s of heating. [36] Inspired by ancient papyrus scrolls, Zhang et al. developed the Chinese national flag locking deployment mechanism and realized the first controlled deployment of the Chinese national flag on Mars. [37] Zeng et al. developed the deployable SMPC flexible solar array system (SMPC-FDS), which successfully completed the on-orbit deployment mission in November 2021 in the Mars remote-sensing orbit, achieving multi-angle shooting of the Chinese national flag by the camera. [38].

In this work, two types of the self-driven curved hinges with different angles of 80° and 115° were designed by epoxy-based SMPCs. Thermomechanical and viscoelastic behaviors of SMPCs were investigated. The mechanical and shape memory properties of hinges were characterized, including three-point bending and cycle shape memory (cycle SM) tests. Specifically, the deployment performance of the hinge driven 350 g object under different heating powers was carried out at $\pm$ 70 °C and 10^3 Pa atmospheric pressure. A staircase-like heating strategy was proposed to satisfy the precise and controllable deployment of the hinge under this environment. In addition, the thermomechanical programming process of the hinges were simulated by finite element analysis (FEA). The developed hinges demonstrated potential application prospects in flap actuator and optical payload rotating platform of the satellite.

2. Design and experiment

2.1. Materials

The hinges were prepared utilizing epoxy-based SMPs, which was synthesized by Leng's research group according to Ref. [30]. The carbon fiber was purchased from Weihai Guangwei Group Co., Ltd (twill woven T300-3 K $\pm$ 45°). As shown in Fig. 1(a), SMPCs was fabricated by vacuum-assisted resin transfer molding (VARTM), consisting of 4 layers of carbon fiber fabrics (the volume fraction of carbon fiber $\sim$ 50 %).

2.2. Thermomechanical properties tests of SMPs/SMPCs

The dynamic mechanical analysis of the epoxy-based SMPs/SMPCs was performed on a DMA tester (DMA Q800®). The sample was heated to 25 °C and then stabilized for 30 min to achieve thermal equilibrium. A preload of 0.001 N and an oscillation frequency of 1 Hz was applied on the rectangular sample (20 mm × 5 mm × 2 mm). Meanwhile, the temperature was heated from 25 °C to 200 °C at the rate of 2.5 °C min^{-1}.

The isothermal static uniaxial tensile tests of SMPCs were characterized at seven different temperatures (25 °C, 50 °C, 75 °C, 100 °C, 125 °C, 150 °C, and 175 °C) by an INSTRON 5569® Testing System with a temperature chamber. The sample with the dimension of 250 mm × 25 mm × 2 mm was placed in the chamber for 30 min before loading to ensure thermal equilibrium. Then each sample was tested following standard ASTM D3039 with a loading rate of 2 mm min^{-1} until failure.

The stress relaxation behaviors of SMPCs were examined at different temperatures (75 °C, 80 °C, 90 °C, 105 °C, 115 °C, 125 °C, 130 °C, 135 °C, 145 °C, 155 °C, 165 °C, 175 °C, 185 °C, and 200 °C) by Zwick-010® testing machine. The relaxation test consisted of two steps. First,
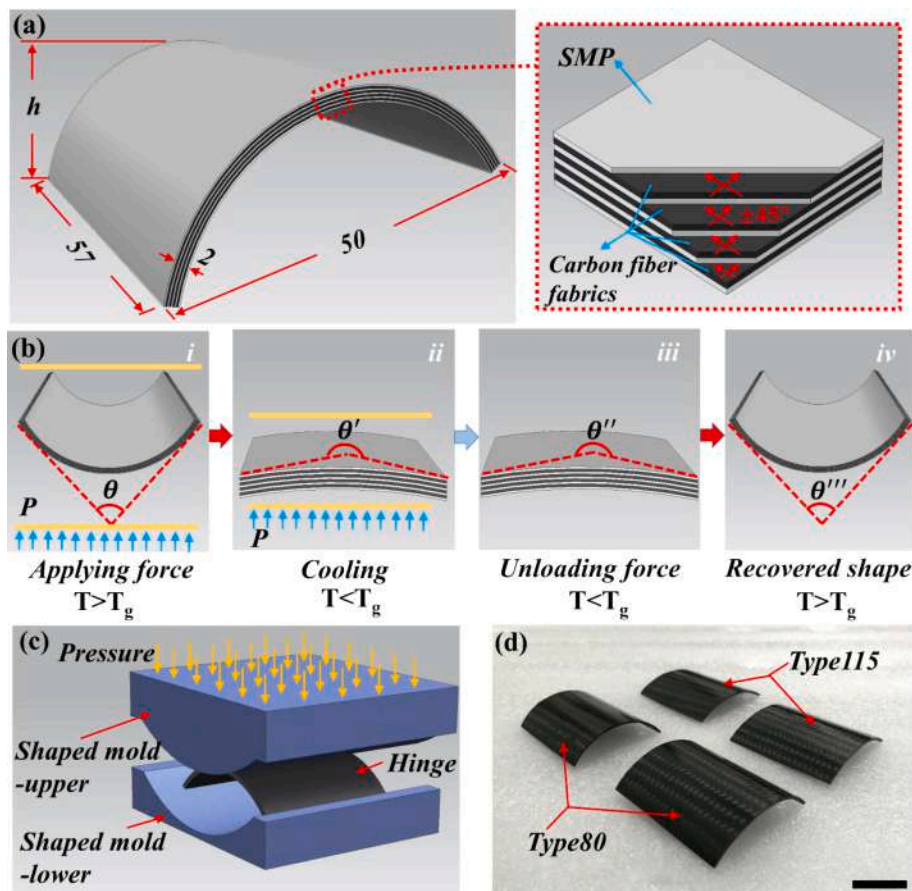

Fig. 1. (a) Dimensions of hinge; (b) Thermomechanical programming process of the self-driven hinge; (c) Programming hinge by shaping molds; (d) Two types of self-driving hinges prepared by VARTM. The scale bar is 25 mm.

the sample was stretched. For temperatures below 115 °C, the sample was stretched by 0.5 mm. Otherwise, it was stretched by 1 mm (2 mm min^{-1}). Second, the deformation was maintained for 1800 s and the stress decay was recorded. Other parameters were the same as isothermal uniaxial tensile test.

2.3. Design and manufacture of self-driven curved hinges

The dimension of the two types of hinges was 57 mm × 5 mm × 2 mm. The thermomechanical programming process of the self-driven curved hinge as shown in Fig. 1(b): (*i*) The curved hinge with initial angle θ was heated above its glass transition temperature (T_g) and the angle was changed to θ' by applying force; (*ii*) Maintained this load and cooled to room temperature; (*iii*) Removed this load and the angle of the hinge was changed to θ''; (*iv*) The hinge was reheated above its T_g and the angle was changed to θ'''. Two types of the self-driven hinge with different θ (80°, 115°) were designed. For the convenience of description, the hinges with $\theta = 80°$ and 115° were represented by Type 80 and Type 115, respectively.

In the programming process, the hinge and shaping molds were placed in an environmental chamber with the temperature of $T_g + 40$ °C for 15 min. Then the hinge and molds were subjected to a pressure of 0.5 MPa, as shown in Fig. 1(c). After cooling (~20 min) and unloading, the temporary shape of the hinge was maintained. It was noteworthy that if the temperature gradient between the molds and the hinge was too high during the programming process, cracks appeared on the surface of the hinge after cooling. Therefore, the shaping molds and hinge were heated together in this work to ensure even temperature transfer. Two types of self-driving hinges prepared by VARTM are shown in Fig. 1(d).

2.4. Thermomechanical properties and shape memory behavior characterization

The bending capabilities of the hinges were investigated by three-point bending tests. The loading method of three-point bending test is shown in Fig. 2, and the loading rate is 2 mm min^{-1}.

Fig. 2. Three-point bending test.

Theoretically, polymers can undergo infinite shape memory recovery cycles. However, previous studies shown that SMPs' shape memory performance decreased with the increase of the number of cycles. The shape memory performance was evaluated in terms of the *n*-th cycle shape fixity ratio ($R_{f,n}$), average and total shape recovery ratio ($R_{r,a,n}$, $R_{r,t,n}$). [31] The shape memory cycle of the hinge was investigated for 15 times. In each cycle, the θ'' of the hinge was measured, then the hinge was placed in an environmental chamber (175 °C) for 5 min, finally the recovery angle was measured after cooling. The surface morphology of the hinge at the last cycle was recorded by the VEGA3 TESCAN® scanning electron microscope (SEM) at an accelerating voltage of 20.0 kV.

Two resistive film heaters with the resistance of 39.7 Ω were attached in parallel to the upper and lower surfaces of the hinge to heat the hinge. It was noteworthy that a layer of aluminum foil was pasted between each heater and the hinge to ensure uniform heat transfer. A layer of polyimide tape was attached to the outer layer of the heater to prevent the electronic components from being damaged. The deployment performance and temperature field distribution of the hinge driving an object with 350 g at the heating power of 39.5 W were characterized by a video camera (Canon DS126571) and infrared camera (InfraTec, VarioCam), respectively.

The deployment performances of Type 80 for driving 350 g object at different heating powers (51.20 W, 48.05 W, 42.05 W, 36.45 W, 31.25 W, and 26.45 W), 10^3 Pa and different temperatures (+70 °C, −70 °C) were also investigated. The experiment was carried out in a space simulated chamber. First, the chamber was evacuated to a pressure of less than 0.1 Pa and dry N$_2$ gas was delivered to reach 10^3 Pa, then the temperature in the chamber was heated to + 70 °C. The procedure of −70 °C test was similar to the + 70 °C, except that liquid nitrogen was used to control the temperature of the chamber during the cooling process. When the temperature of the thermocouple pasted on the hinge surface reached the target temperature (+70 °C/-70 °C), it was maintained for 1 h before testing to ensure thermal equilibrium. The hinge completion deployment time was recorded. In addition, the stiffness of SMPCs decreased with the increase of heating time, causing the object to fall back. This fall-back time was also recorded in the + 70 °C test. Three hinges were tested under each test condition.

3. Results and discussion

3.1. DMA test of SMPs and SMPCs

Fig. 3 exhibits the temperature dependence of storage modulus (E_s) and tan δ of the epoxy-based SMPs/SMPCs. The E_s of SMPCs was higher
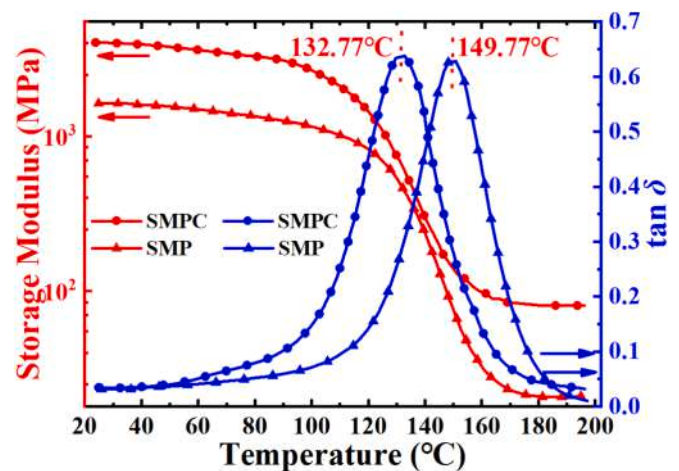

Fig. 3. Temperature dependence curves of the storage modulus and tan δ of SMPs and SMPCs.

than SMPs at each test temperature due to the enhanced of fibers. It was observed that E_s had strong temperature dependence and the change rate $\sim$ 97 %. When SMPs and SMPCs were in the glassy phase at low temperature (T_l = 27 °C), the E_s was 1628.28 MPa and 4037.08 MPa, respectively. When SMPs and SMPCs were in the rubbery phase at high temperature (T_h = 200 °C), the E_s was 20.94 MPa and 80.87 MPa, respectively. In addition, it can also be observed that the temperature corresponding to the peak of tan δ curve of SMPCs was lower than that of SMPs, i.e., T_g of SMPs and SMPCs was 149.77 °C and 132.77 °C, respectively.

3.2. Thermomechanical properties of SMPCs

Isothermal uniaxial tensile stress–strain curves and the Young's modulus of SMPCs at seven different temperatures are shown in Fig. 4(a) and Table 1, respectively. The Young's modulus and strength of SMPCs decreased significant with the increase of temperature. The strength and Young's modulus of SMPCs were 159.80 MPa and 3.72 GPa at 25 °C, respectively. However, the strength and Young's modulus of SMPCs were 10.41 MPa and 0.20 GPa, which decreased by 93.5 % and 95.6 % at 175 °C. It was worth noting that the composite in rubbery phase at 150 °C and 175 °C, leaded to similar mechanical properties of the composite at these temperatures (strength: 14.73 MPa at 150 °C, 10.41 MPa at 175 °C; Young's modulus: 0.21 GPa at 150 °C, 0.20 GPa at 175 °C). This was in good agreement with the result that the storage modulus kept constant at 150 °C $\sim$ 200 °C in DMA curves. In general, the material had high strength and modulus in the glassy phase, which was suitable for load-bearing. In the rubbery phase, the material was soft and flexible, which was suitable for programming.

The relaxation modulus was obtained by stress relaxation testing,

Table 1
Young's modulus and strength values of SMPCs at different temperatures.

Temperatures (°C)	25	50	75	100	125	150	175
Young's modulus (GPa)	3.72	2.55	2.26	0.68	0.31	0.21	0.20

which was one of the most important methods to investigate the viscoelastic property of the material. The relaxation modulus calculated by relaxation stress depends on time and temperature is shown in Fig. 4 (b). Relaxation modulus of SMPCs showed a significant dependence on time in the glass transition temperature region. The dependence of the relaxation modulus on time was less pronounced at the temperature far from the transition region. It can be observed that the relaxation modulus of SMPCs varied greatly between 75 °C and 125 °C. The change of the relaxation modulus of the material was not obvious at 145 °C $\sim$ 200 °C.

3.3. Thermomechanical behavior of self-driven hinges

The displacement-force curves obtained by the three-point bending test at different temperatures are shown in Fig. 4(c)$\sim$(d). The variable stiffness of SMPCs caused it to exhibit high load-carrying capacity at low temperature and low load carrying capacity at high temperature. Taking Type 80 as an example, the maximum load of the hinge at 25 °C and 175 °C was 423.91 N and 26.28 N, respectively. The cross-section of the hinge designed in this work was arch-shaped and the bending capability of the structure with large curvature was high. Therefore, the maximum load of Type 80 was higher than Type 115 at each test temperature. For example, the maximum load of Type 80 and Type 115 was 429.31 N and 141.17 N at 25 °C, respectively. Interestingly, the hinge was able to
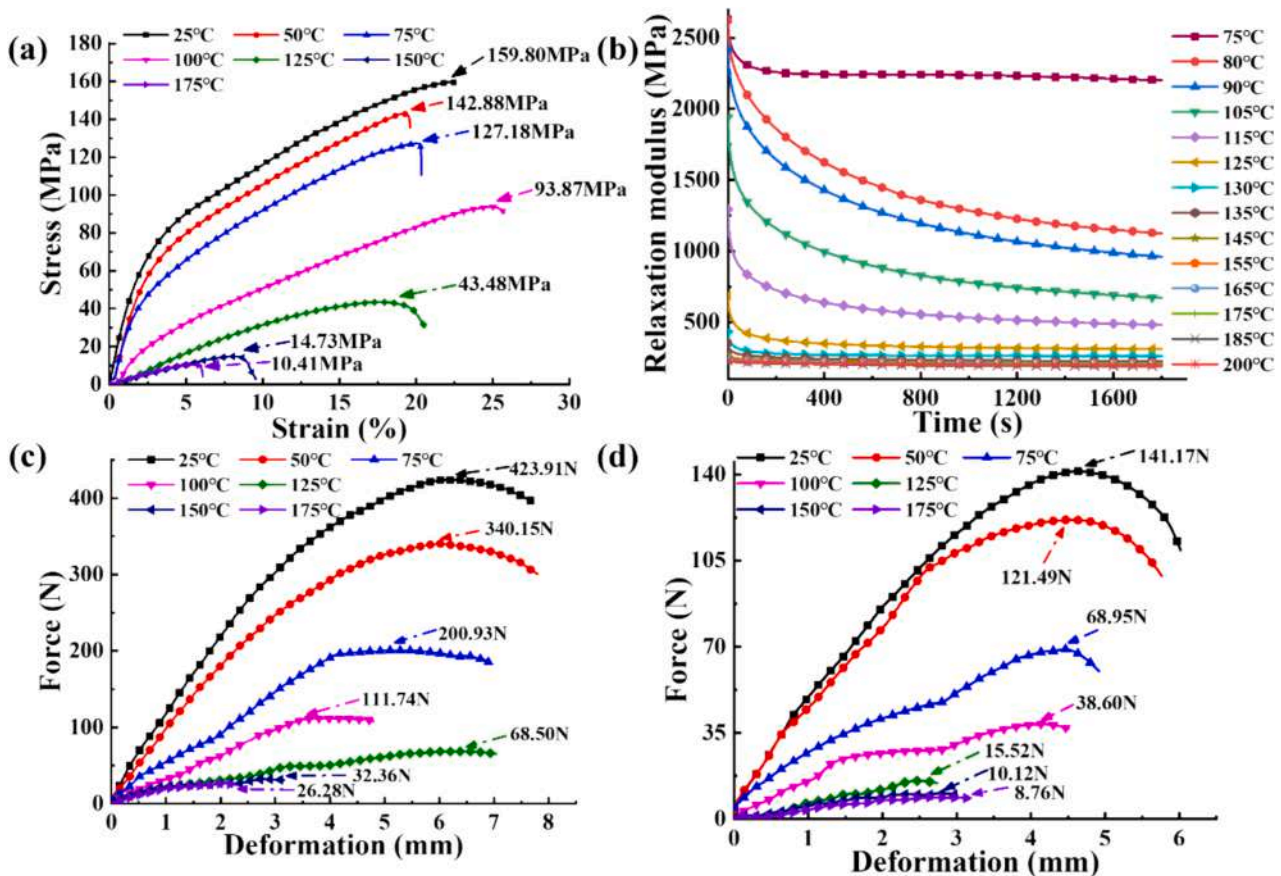

Fig. 4. Thermomechanical properties of SMPCs: (a) isothermal static uniaxial tensile test; (b) stress relaxation test; three-point bending test of (c) Type 80 (d) Type 115.

recover to its original shape without fracture after unloading. The reasons could be divided into two cases: when SMPCs were in glassy phase, this phenomenon was caused by elastic deformation. When SMPCs were in rubbery phase, the recovery was caused by elastic deformation and shape memory recovery.

3.4. Cyclic SM

The $R_{f,n}$, $R_{r,a,n}$, and $R_{r,t,n}$ were used to evaluate the cyclic SM performance of SMPCs, which were defined as follows:

$$R_{f,n} = \frac{\theta_u}{\theta_p} \times 100\% \quad (n = 1, 2, 3\ldots) \tag{1a}$$

$$R_{r,a,n} = \frac{\theta_u - \theta_f(n)}{\theta_u - \theta_f(n-1)} \times 100\% \quad (n = 1, 2, 3\ldots) \tag{1b}$$

$$R_{r,t,n} = \frac{\theta_u - \theta_f(n)}{\theta_u} \times 100\% \quad (n = 1, 2, 3\ldots) \tag{1c}$$

where θ_u was the angle measured before reheating after removing the pressure; θ_p was the prescribed rotation angle; θ_f was the angle of the hinge after reheating; n was the cycle number. $R_{r,a,n}$ described the shape memory behavior in the current SM cycle, while $R_{r,t,n}$ described the SM behavior of the current state to its original state. The calculation results of the three parameters in Eq. 1 are shown in Fig. 5(a). It can be seen that $R_{f,n}$ decreased with the number of the cycle. $R_{f,n}(n = 15)$ of Type 80 and Type 115 at the last cycle were 91.5 % and 95 %, respectively. $R_{r,a,n}$ ($n = 15$) almost remained constant (nearly 99 %). $R_{r,t,n}$ decreased slightly with the number of cycles but $R_{r,t,n}(n = 15)$ remained above 97 %.

There was little damage on the upper surface of Type 80 and Type 115 after 15 cycles SM. Fig. 5(b) shows the damage of the Type 80 surface at different magnifications. The red rectangle in the *i*th image of Fig. 5(b) is the observation place. The *iii*th and *iv*th of Fig. 5(b) show that the matrix had cracks and some broken fibers were pulled out of the matrix. The existence of damage also leaded to the reduction of shape memory performance of hinges after cycle SM.

3.5. Deployment performance of the hinge in different environments

Fig. 6(a) ~ 6(b) show the deployment process of 350 g object driven by Type 80 and the distribution of temperature field on the hinge surface at the heating power of 39.5 W. The deployment time of Type 80 was 57 s, which can drive the object to rotate 76.66°. The temperature distribution on the surface of the hinge was uniform, and the temperature of the deformed part of the hinge was higher. In the deployment process, the middle part of the hinge recovered from plane to curve, which was the main source of driving force. After heating 12 s, the hinge was deployed and its maximum surface temperature was 105 °C. The maximum temperature of the hinge surface was 205.5 °C after deployment. The recovery of Type 80 was faster in 12 s ~ 23 s, while the recovery was slower in 23 s ~ 57 s. The reason for this phenomenon might be that the stiffness of the hinge decreased with the increase of the temperature, and the rotation angle of the hinge changed slowly due to gravity. Fig. 6(c) ~ 6(d) demonstrate the recovery process and temperature distribution of Type 115 at 39.5 W heating power. The deployment time of Type 115 was 60 s, which can drive the object to rotate 30.45°. The temperature distribution of Type 115 was similar to that of Type 80. The maximum temperature of the hinge was 207.50 °C after deployment (Fig. 6(e)).

Fig. 6(f) exhibits the deployment test results of Type 80 in the environment of ± 70 °C and 10^3 Pa atmospheric pressure. The hinge deployment time decreased with the increase of power. For example, the deployment time of the hinge was 39.33 s (31.25 W) and 26.33 s (51.2 W) at + 70 °C, respectively. In addition, the deployment time of the hinge at −70 °C was higher than that at + 70 °C. When the heating power was 51.2 W, the deployment time of the hinge at + 70 °C and −70 °C was 26.33 s and 71.67 s, respectively. The fall back time became shorter with the increase of heating power at + 70 °C. When the power was 51.2 W, the fall back time of the hinge was 127.33 s. However, when the heating power was 26.45 W, the hinge did not fall back after heating 15 min. A stairway-like heating strategy for the hinge deployed in the environment of −70 °C ~ +70 °C and 10^3 Pa can be obtained according to the deployment time at −70 °C and the fall back time at + 70 °C. P was denoted as heating power, the heating time of 48.05 W ≤ P ≤ 51.20 W, 42.05 W ≤ P < 48.05 W, 36.45 W ≤ P < 42.05 W, 31.25 W ≤ P < 36.45 W, and 26.45 W ≤ P < 31.25 W was 100 s, 110 s, 120 s, 135 s, and
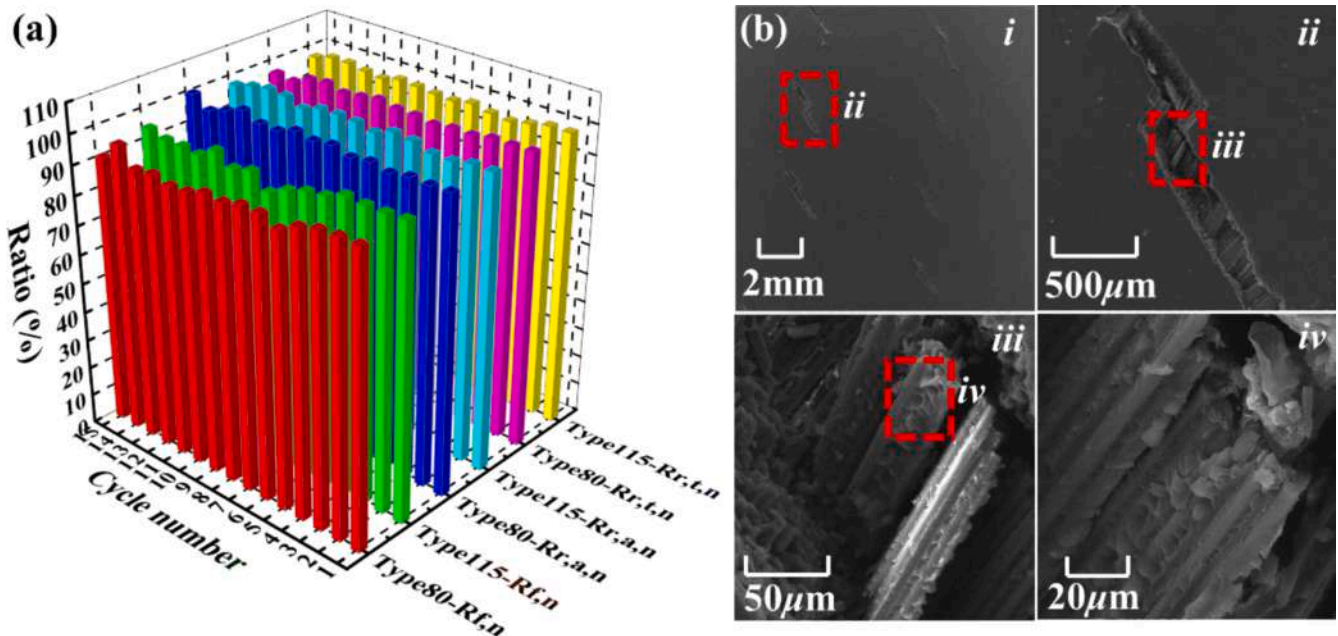

Fig. 5. (a) Relationship between shape memory behavior parameters and number of cycles; (b) SEM images of different magnifications of Type 80 surface at the last cycle, *i*th: magnification of 15×, *ii*th: magnification of 116×, *iii*th: magnification of 1150×, *iv*th: magnification of 2100 × .
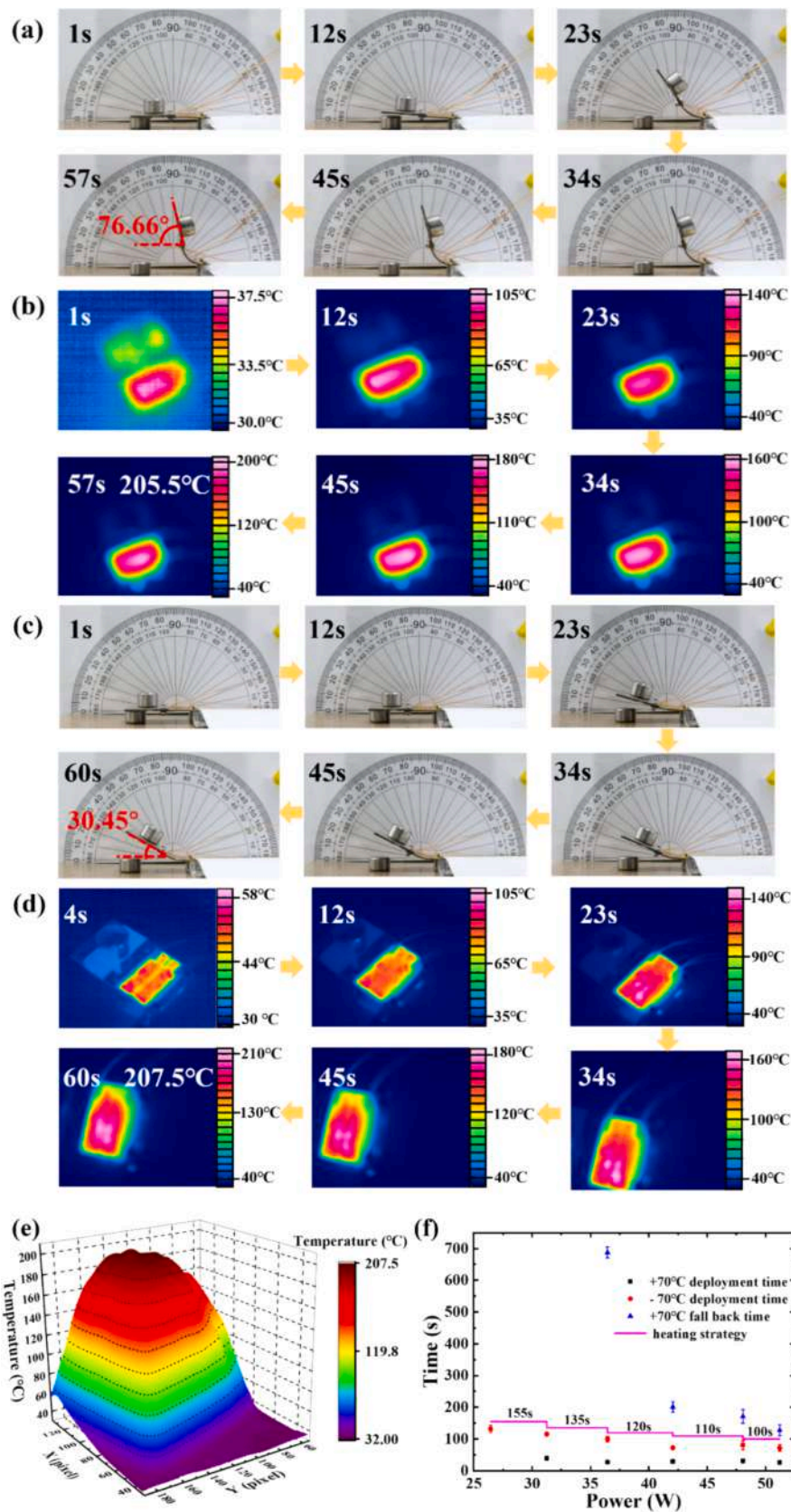
Fig. 6. (a) The deployment process and (b) surface temperature distribution of 350 g object driven by Type 80 at 39 W heating power; (c) the deployment process and (d) surface temperature distribution of 350 g object driven by Type 115 at 39 W heating power; (e) surface temperature distribution of Type 115 after heating 60 s; (f) deployment time and heating strategy of Type 80 at 10^3 Pa under different temperatures and heating powers.

155 s, respectively. The heating strategy not only satisfied the object not fall back but also ensured that the hinge complete deployment in the environment of −70 °C ∼ +70 °C and 10^3 Pa, as shown in Fig. 6(f).

Fig. 7 exhibits the Ashby plot comparison results of the glass transition temperature, the deployment time and shape recovery ratio of the SMPCs hinges developed in this work with the existing works. The developed hinges in this work exhibited higher glass transition temperatures, higher shape recovery ratio and faster deployment properties. Since the deployment performance of SMPCs structures was temperature dependent, the higher T_g enabled SMPCs hinges to be applied at higher orbital altitudes, which were not affected by the ambient temperature, leading to earlier deployment of the structures. Compared to the hinges which required long heating times to complete deployment, the developed hinges in this work enabled rapid deployment, thus conserving resources on the satellite. Meanwhile, higher shape recovery ratio allowed the space deployment structure to be deployed with high precision and carried out on-orbit work.

4. Finite element analysis

The finite element simulation of the thermomechanical cycle of two types of hinges was implemented in the commercial finite element software ABAQUS standard 6.14® (3DS Dassault Systèmes, France). The multi-branch constitutive model was utilized to describe the time–temperature dependent viscoelastic behavior of SMPCs. Fig. 8(a) shows the 1D representation of the multi-branch rheological model, which consisted of a balanced branch of an elastic spring and several non-balanced branches in parallel connected in series by a spring and a dashpot. The multi-branch constitutive model directly reflects the stress relaxation behavior of materials in the time domain. The stress relaxation modulus is defined as follows: [32]

$$E(t) = E_\infty + \sum_{i=1}^{n} E_i e^{\left(-\frac{t}{\tau_i}\right)} \tag{2}$$

where E_∞ represents the equilibrium modulus of SMPCs, E_i and τ_i are the related parameters of Prony series, representing elastic modulus and relaxation time of the ith non-equilibrium branch, respectively.

In this work, the relaxation modulus of SMPCs at different temperatures and time domains was obtained by the time–temperature superposition principle (TTSP). The relaxation behavior of SMPCs at any temperature can be obtained by reference temperature, which is defined as follow:

$$E(t, T_{ref}) = E(\alpha_T t, T) \tag{3}$$

where α_T is TTSP shifting factor.

Follow O'Connell and McKenna to calculate the effect of T on the viscoelastic behavior of material depending on whether T is higher or lower than shifting temperature (T_s). [33] For T below T_s, α_T satisfies Arrhenius-Type behavior: [34]

$$\ln\alpha_T(T) = -\frac{AF_c}{k_b}\left(\frac{1}{T} - \frac{1}{T_g}\right) \tag{4}$$

Conversely, for the T near or larger than T_s, α_T can be calculated using the Williams-Landel-Ferry (WLF) equation: [35]

$$\log\alpha_T(T) = -\frac{C_1\left(T - T_{ref}\right)}{C_2 + \left(T - T_{ref}\right)} \tag{5}$$

where A, C_1, and C_2 are material constants, F_c is configurational energy and k_b is Boltzmann's constant. The value T_{ref} is generally 10 °C lower than T_g. Fig. 8(b) shows α_T as a function of temperature T. The parameters of TTSP were determined by fitting the discrete experimental data with the theoretical prediction model of Eq. (4) ∼ 5 and T_s was determined by the intersection of the two curves. The related parameters are shown in Table 2.

Fig. 8(c) shows the relaxation modulus master curve of SMPCs, which spans about 10 times, representing the actual relaxation behavior of SMPCs over a long period of time (∼571 years) at 125 °C. According to the Prony series of multi-branch model, the experimental master curve can be accurately reproduced. Here, the number of unbalanced chains of the multi-branch model is $n = 16$, and the parameters are shown in Table 2.

Type 80/Type 115 meshed with 756/812 shell 4-node quadrilateral elements (S4R). The thermomechanical process of the hinge was accomplished by utilizing five steps (*Initial* step and four *Visco* steps) in the solution module of ABAQUS (as shown in Table 2.). In the *Initial* step, the temperature of FE model was defined by a predefined field, which was constant through the region (180 °C). In addition, a fixed boundary condition (BC) was imposed on the one side of the hinge (U$_1$ = U$_2$ = U$_3$ = UR$_1$ = UR$_2$ = UR$_3$ = 0). In the first *Visco* step, a torsional load was applied to a reference point, which established coupling constraints with the other side of the model. This torsional load was inactive (i.e., unloaded) in the 3rd and 4th *Visco* steps.

Notice that the temperature field of this step propagates the *Initial* step. The modified predefined field linearly reduced the temperature to 20 °C in the second *Visco* step and propagated to the third *Visco* step. In the fourth *Visco* step, the time period and time–temperature amplitude curve were based on the deployment time and the infrared camera test results. It was obvious that the heat of the hinge was concentrated in the middle part of the hinge during heating in Fig. 6(b) and (d), which was
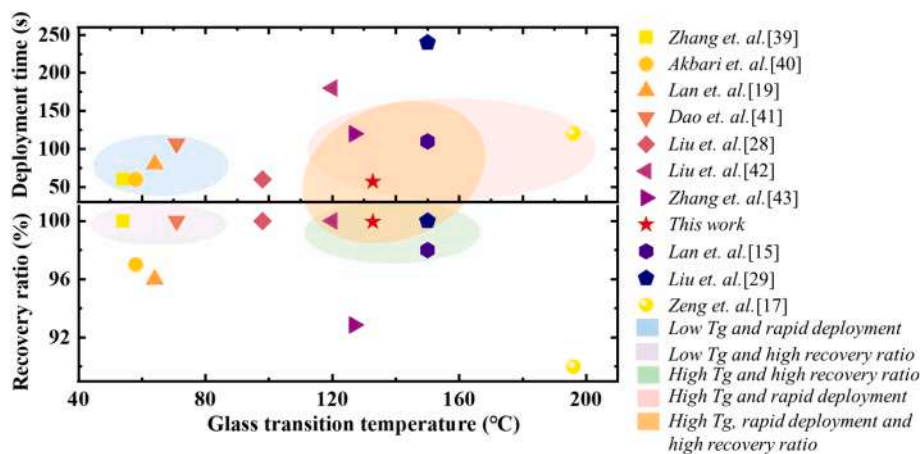

Fig. 7. The comparison results of the deployment performance of the developed SMPCs hinges with other literatures (See above-mentioned references for further information.).
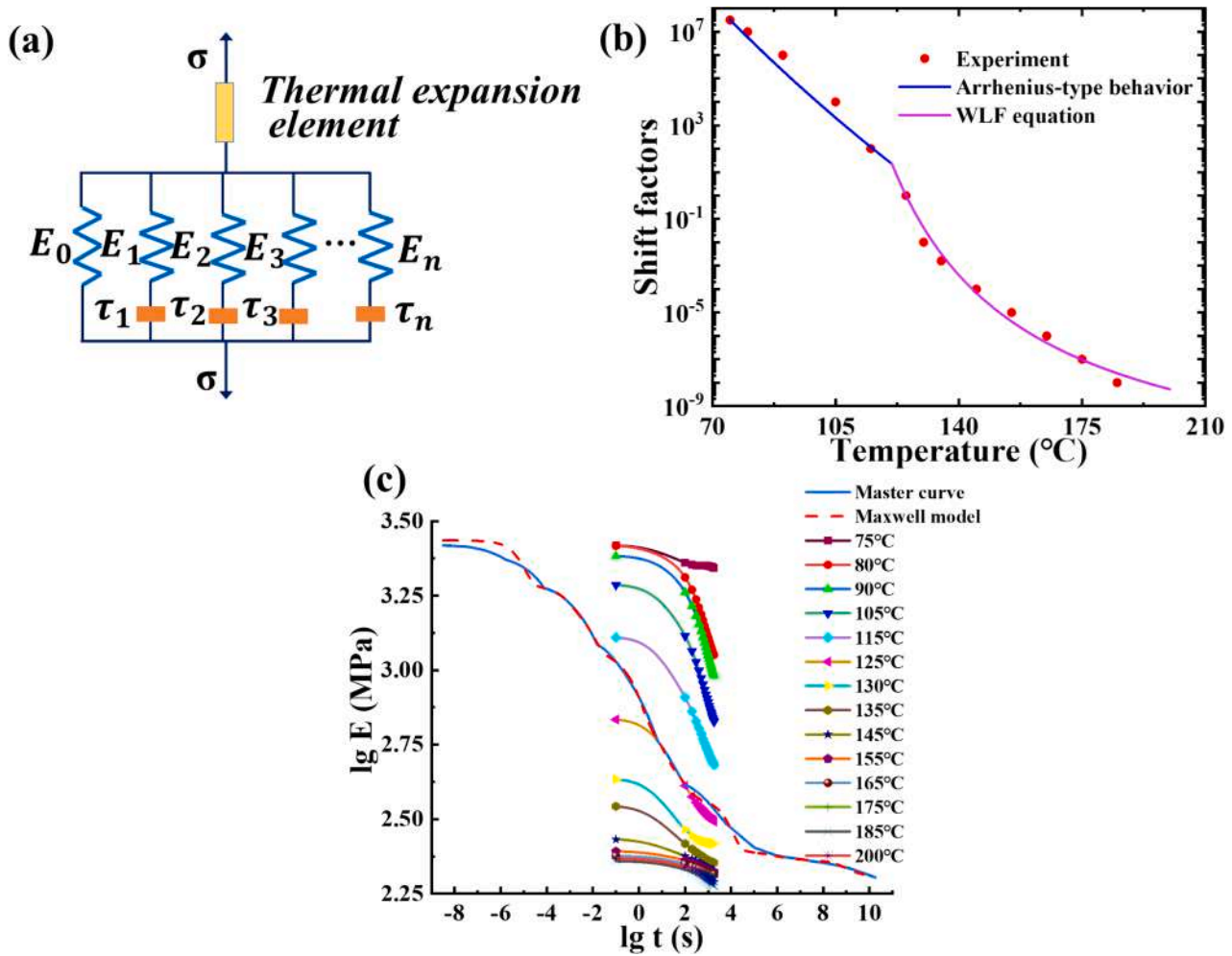
Fig. 8. (a) 1D representation of the multi-branching model; (b) Shifting factors at different temperatures; (c) The experimental and predicted of the master curve at 125 °C.

Table 2
Material properties and analysis steps of FE analysis.

Parameters of non-equilibrium branches					
$g_1 \sim g_{16}$(MPa)	0.2973, 0.0044, 01090, 0.1664, 0.0277, 0.1448, 0.0702, 0.0437, 0.0003, 0.0457, 0.0009, 0.0037, 0.0011, 0.0003, 0.0074, 0.0032				
$\tau_1 \sim \tau_{16}$(s)	10^{-5}, 10^{-4}, 10^{-3}, 10^{-2}, 10^{-1}, 1, 10, 100, 10^3, 10^4, 10^5, 10^6, 10^7, 10^8, 10^9, 10^{10}				
Parameters in TTSP					
T_S	121 °C		C_2		42.03
C_1	12.92		AF_c/k_b		−42300.37
FE steps, BC, and load					
step	Initial step	First step	Second step	Third step	Forth step
Procedure	/	*Visco*	*Visco*	*Visco*	*Visco*
Time period		100 s	200 s	1 s	57 s for Type 80
					60 s for Type 115
Boundary condition	Created ($U_1 = U_2 = U_3 = UR_1 = UR_2 = UR_3 = 0$)	propagated	propagated	propagated	propagated
	/	Created	propagated	Inactive	Inactive
Predefined Field	Created (Constant through region = 180 °C)	propagated	Modified (Lower to 20 °C)	propagated	Modified (Reheated by amplitude curve)

also the deformation position. The time–temperature curve was approximated to the maximum temperature of the hinge at each time in Fig. 6(b) and (d).

Fig. 9(a) and (b) show the Mises stress distribution on the hinge surface during deployment of Type 80 and Type 115, respectively. The corner of the hinge appeared higher stress because of the stress concentration. The deformation of Type 80 was higher than that of Type 115, which resulted in that the storage stress of Type 80 was higher than

that of Type 115. Storage stress was released by reheating at the fourth *Visco* step.

5. Potential applications

Deployable structures have a wide range of applications in aerospace, such as solar arrays, multi-angle imaging systems and antennas. The designed hinge in this work had the advantages of the lightweight
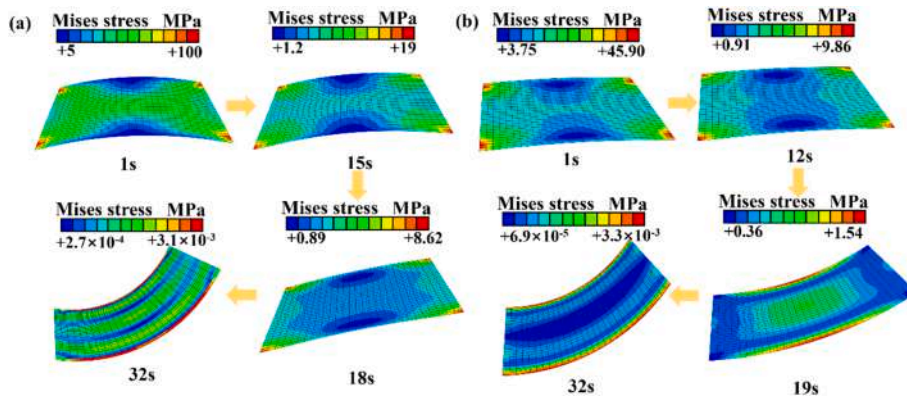
Fig. 9. Mises stress distribution on hinge surface during deployment: (a)Type 80, (b) Type 115.

and large driving force. It is expected to have promising application prospects on flap actuator and optical payload rotating platform of the satellites.

The wing is one of the important components of the aircraft. It is equipped with flaps and ailerons to improve take-off/landing performance and lateral control of aircraft. The aerodynamic configuration of the aircraft is optimized by controlling the rotation of these components during flight. However, the existing flap actuator has a complicated mechanical structure and a large mass. For example, the flap is usually equipped with a slide rail structure to drive its rotation. The self-driven intelligent curved hinge can be used to replace the conventional flap actuator, which can not only reduce the weight of the aircraft but also can reduce flight costs and energy. The hinge will be in its temporary shape during the cruising of the aircraft, as shown in Fig. 10(a). During the take-off and landing phases, the hinge will be heated to achieve the rotation of the flap, as shown in Fig. 10(b).

The self-driven hinge can also be connected with the camera to form the optical payload rotating platform to realize the monitor of satellite state and self-timer. As shown in Fig. 11(a), the hinge in its temporary shape will be launched with the satellite to save the internal space of the rocket. The hinge will be heated when the satellite reaching the designated orbit. Then the hinge drives the camera to rotate to complete the optical test task of observing the deployment status of solar array and self-timer of satellite, as shown in Fig. 11(d).

6. Conclusion

In this work, two types of SMPCs self-driven hinges were designed and analyzed. Firstly, the thermoviscoelastic properties of SMPCs at different temperatures were obtained by DMA, isothermal static uniaxial tension and stress relaxation tests. It was found that SMPCs had a strong time–temperature dependence. Three-point bending tests at different temperatures showed that the bending strength of Type 80 was higher than that of Type 115. The designed hinges had an excellent cycle SM performance. The $R_{r,t,n}$ ($n = 15$) of the hinge was over 97 % after 15
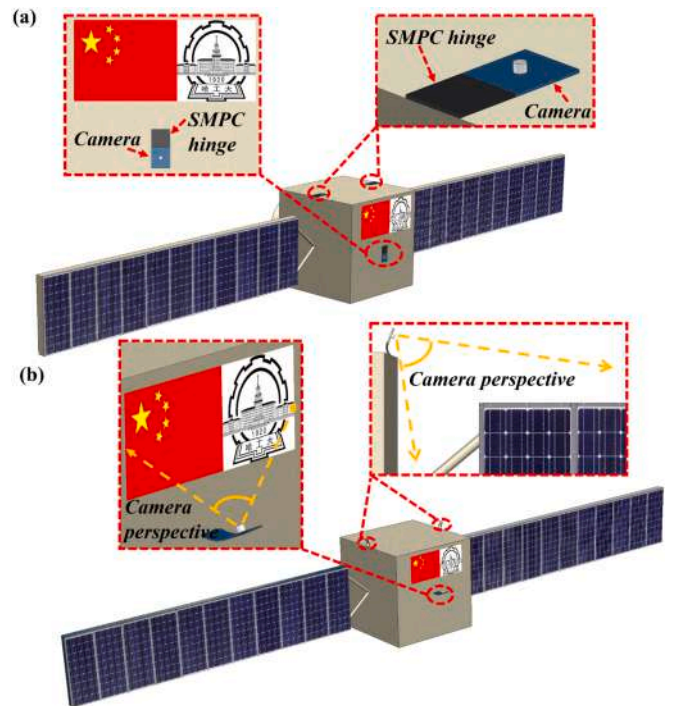

Fig. 11. Self-driven hinge as optical payload rotation platform of satellite completes optical test task: (a) launch status; (b) deployment status.

cycles. When the heating power was 39.5 W, Type 80 and Type 115 can drive the object (350 g) to rotate 76.66° and 30.45° respectively after heating ~ 60 s. The deployment time of hinge decreased with the increase of heating power in the deployment test of Type 80 in the environment of ± 70 °C and 10^3 Pa. A stairway-like heating strategy was
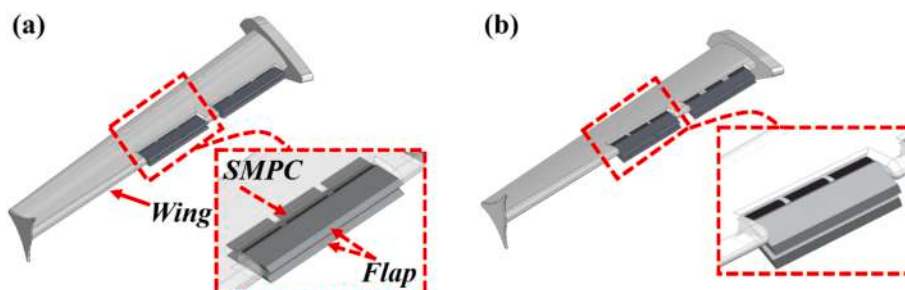

Fig. 10. Self-driven hinge as a flap actuator to drive the flap rotation (a) cruise phase; (b) take-off or landing phase.

proposed to satisfy the accurate and controllable deployment of the hinge at different powers. In addition, the process of hinge deployment was analyzed by finite element simulation. The self-driving hinge have potential applications in the fields of flap actuator and optical payload rotating platform of the satellites.

CRediT authorship contribution statement

Xiaozhou Xin: Writing – review & editing, Writing – original draft, Visualization, Validation, Methodology, Investigation, Conceptualization. **Cheng Lin:** Methodology, Investigation. **Bingxun Li:** Software, Methodology. **Chengjun Zeng:** Investigation, Methodology. **Liwu Liu:** Writing – review & editing, Validation, Supervision. **Yanju Liu:** Writing – review & editing, Visualization, Validation, Supervision. **Jinsong Leng:** Writing – review & editing, Validation, Supervision.

Declaration of competing interest

The authors declare that they have no known competing financial interests or personal relationships that could have appeared to influence the work reported in this paper.

Data availability

Data will be made available on request.

Acknowledgments

References

[1] Delaey J, Dubruel P, Van Vlierberghe S. Shape-memory polymers for biomedical applications. Adv Funct Mater 2020;30:1909047.

[2] Lendlein A, Gould OEC. Reprogrammable recovery and actuation behaviour of shape-memory polymers. Nat Rev Mater 2019;4:116–33.

[3] Xia YL, He Y, Zhang FH, Liu YJ, Leng JS. A review of shape memory polymers and composites: Mechanisms, materials, and applications. Adv Mater 2021;33: 2000713.

[4] Zhang H, Wang D, Wu NN, Li CH, Zhu CZ, Zhao N, et al. Recyclable, self-healing, thermadapt triple-shape memory polymers based on dual dynamic bonds. ACS Appl Mater Interfaces 2020;12:9833–41.

[5] Zhao Q, Qi HJ, Xie T. Recent progress in shape memory polymer: New behavior, enabling materials, and mechanistic understanding. Prog Polym Sci 2015;49–50: 79–120.

[6] Liang RX, Yu HJ, Wang L, Wang N, Amin BU. NIR light-triggered shape memory polymers based on mussel-inspired iron-catechol complexes. Adv Funct Mater 2021;31:2102621.

[7] Zhao W, Li N, Liu LW, Leng JS, Liu YJ. Mechanical behaviors and applications of shape memory polymer and its composites. Appl Phys Rev 2023;10:011306.

[8] He X, Lin YC, Ding YC, et al. Reshapeable, rehealable and recyclable sensor fabricated by direct ink writing of conductive composites based on covalent adaptable network polymers. Int J Extr Manuf 2022;4:015302.

[9] Zhan ZH, Chen L, Duan HG, et al. 3D printed ultra-fast photothermal responsive shape memory hydrogel for microrobots. Int J Extr Manuf 2022;4:015401.

[10] Lyu ZY, Wang JL, Chen Y. 4D printing: interdisciplinary integration of smart materials, structural design, and new functionality. Int J Extr Manuf 2023;5: 032011.

[11] Ren HP, Ouyang YW, Xiao SL, Xu WL, Liu Y. Shape memory property and mechanism of the knitting-fabric reinforced epoxy composites subjected to tensile loading. Compos Sci Technol 2022;230:109724.

[12] Ren ZK, Liu LW, Liu YJ, Leng JS. Electric power repair tools made of shape memory composites: Analysis and investigation. Compos Struct 2020;252:112712.

[13] Xu LD, Zhao JT, Shi MF, Liu JB, Wang ZQ. Thermodynamic properties of TPI shape memory polymer composites reinforced by GO/SiO modified carbon fiber. Compos Sci Technol 2022;226:109551.

[14] Lan X, Liu LW, Pan CT, Hou GH, Li FF, Liu ZX, et al. Smart space deployable truss based on shape-memory releasing mechanisms and actuation laminates. J Spacecr Rocket 2023;60:1085–99.

[15] Lan X, Liu LW, Pan CT, Li FF, Liu ZX, Hou GH, et al. Smart solar array consisting of shape-memory releasing mechanisms and deployable hinges. AIAA J 2021;59: 2200–13.

[16] Xin XZ, Liu LW, Liu YJ, Leng JS. Mechanical models, structures, and applications of shape-memory polymers and their composites. Acta Mech Solida Sin 2019;32: 535–65.

[17] Zeng CJ, Liu LW, Du Y, Yu M, Xin XZ, Xu PL, et al. Space-deployable device based on shape memory cyanate ester composites. Compos Commun 2023;42:101690.

[18] Moening CJ. Pyrotechnic shock flight failures. Institute of Environmental Sciences Pyrotechnic Shock Tutorial Program , 31st Annual Technical Meeting , 1985.

[19] Lan X, Liu YJ, Lv HB, Wang XH, Leng JS, Du SY. Fiber reinforced shape-memory polymer composite and its application in a deployable hinge. Smart Mater Struct 2009;18:024002.

[20] Beavers F, Munshi N, Lake M, Maji A, Qassim K, Carpenter B, Rawal S. Design and Testing of an Elastic Memory Composite Deployment Hinge for Spacecraft. 43rd AIAA/ASME/ASCE/AHS/ASC Structures, Structural Dynamics, and Materials Conference, 2002.

[21] Francis W, Lake M, Mallick K, Freebury G, Maji A. Development and testing of a hinge/actuator using elastic memory composites. 44th AIAA/ASME/ASCE/AHS/ ASC structures, structural dynamics, and materials conference. 2003.

[22] Dao TD, Goo NS, Yu WR. Blocking force measurement of shape memory polymer composite hinges for space deployable structures. J Intell Mater Syst Struct 2018; 29:3667–78.

[23] Campbell D, Lake M, Scherbarth M, Nelson E, Six R. Elastic Memory Composite Material: An Enabling Technology for Future Furlable Space Structures. 46th AIAA/ASME/ASCE/AHS/ASC Structures, Structural Dynamics and Materials Conference.2005.

[24] Li FF, Liu LW, Lan X, Wang T, Li XY, Chen FL, et al. Modal analyses of deployable truss structures based on shape memory polymer composites. Int J Appl Mech 2016;8:1640009.

[25] Fang H, Shook L, Lin J, Pearson J, Moore J, A Large and High Radio Frequency Deployable Reflector, 53rd AIAA/ASME/ASCE/AHS/ASC Structures, Structural Dynamics and Materials Conference
20th AIAA/ASME/AHS Adaptive Structures Conference
14th AIAA, 2012.

[26] Keller P, Lake M, Codell D, Barrett R, Taylor R, Schultz M. Development of elastic memory composite stiffeners for a flexible precision reflector. In: 47th AIAA/ ASME/ASCE/AHS/ASC structures, structural dynamics, and materials conference 14th AIAA/ASME/AHS adaptive structures conference 7th. 2006.

[27] Chen Q, Yao Z, Hou Y, Fang H, Design and Testing of a Space Deployable Mechanism, 4th AIAA Spacecraft Structures Conference, 2017.

[28] Liu TZ, Liu LW, Yu M, Li QF, Zeng CJ, Lan X, et al. Integrative hinge based on shape memory polymer composites: Material, design, properties and application. Compos Struct 2018;206:164–76.

[29] Liu ZX, Li QF, Bian WF, Lan X, Liu YJ, Leng JS. Preliminary test and analysis of an ultralight lenticular tube based on shape memory polymer composites. Compos Struct 2019;223:110936.

[30] Leng JS, Wu XL, Liu YJ. Effect of a linear monomer on the thermomechanical properties of epoxy shape-memory polymer. Smart Mater Struct 2009;18:095031.

[31] Yu K, Li H, McClung AJW, Tandon GP, Baur JW, Qi HJ. Cyclic behaviors of amorphous shape memory polymers. Soft Matter 2016;12(13):3234–45.

[32] Al Azzawi W, Epaarachchi JA, Islam M, Leng JS. Implementation of a finite element analysis procedure for structural analysis of shape memory behaviour of fibre reinforced shape memory polymer composites. Smart Mater Struct 2017;26: 125002.

[33] O'Connell PA, McKenna GB. Arrhenius-type temperature dependence of the segmental relaxation below T-g. J Chem Phys 1999;110(22):11054–60.

[34] Di Marzio EA, Yang AJM. Configurational entropy approach to the kinetics of glasses. J Res Nat Inst Stand Technol 1997;102:135–57.

[35] Williams ML, Landel RF, Ferry JD. The temperature dependence of relaxation mechanisms in amorphous polymers and other glass form liquids. J Am Chem Soc 1995;77(14):3701–7.

[36] Lan X, Liu L, Zhang F, Liu Z, Wang L, Li Q, et al. World's first spaceflight on-orbit demonstration of a flexible solar array system based on shape memory polymer composites. Sci China Technol Sci 2020;63:1436–51.

[37] Zhang D, Liu LW, Xu PF, Zhao YZ, Li QF, Lan X, et al. World's first application of a self-deployable mechanism based on shape memory polymer composites in Mars explorations: ground-based validation and on-Mars qualification. Smart Mater Struct 2022;31:115008.

[38] Zeng CJ, Liu LW, Du Y, Yu M, Xin XZ, Liu TZ, et al. A shape-memory deployable subsystem with a large folding ratio in China's Tianwen-1 mars exploration mission. Engineering 2023;28:49–57.

[39] Zhang B, Li H, Cheng J, et al. Mechanically robust and UV-curable shape memory polymers for digital light processing based 4D printing. Adv Mater 2021;33: 2101298.

[40] Akbari S, et al. Enhanced multimaterial 4D printing with active hinges. Smart Mater Struct 2018;27:065027.

[41] Dao TD, et al. Design, fabrication, and bending test of shape memory polymer composite hinges for space deployable structures. J Intell Mater Syst Struct 2018; 29:1560–74.

[42] Liu Z, Lan X, Bian W, et al. Design, material properties and performances of a smart hinge based on shape memory polymer composites. Compos B Eng 2020;193: 108056.

[43] Zhang D, et al. Synchronous deployed design concept triggered by carbon fibre reinforced shape memory polymer composites. Compos Struct 2022;290:115513.